PART II

Nuclear Emission Holography

A promising technique for the study of low-dimensional structures

Chapter 8

Introduction to Nuclear Holography

In the history of mankind, humans have always felt the urge to record their perceptions and to describe the world around them either in written text or in a visual presentation such as a drawing, a painting or a photo.

However, in all conventional recording techniques, such as photography, a flat picture of a three-dimensional scene is recorded. All information on the third dimension (depth) is lost. What is recorded on a photographic plate is merely the intensity distribution in the original scene. As a result, all information on the relative phases of the light waves from different points or, in other words, information about the relative optical paths to different parts of the object, is lost.

The unique characteristic of holography is the idea of recording the complete wave field, i.e., both the amplitude and the phase of the light waves scattered by the object. Since all recording media respond only to the intensity, it is necessary to convert the phase information into variations of intensity. This is done by using coherent illumination, as shown in figure 8.1, and adding a reference plane or spherical wave to the wave scattered by the object.
What is recorded on the photographic plate is the interference pattern due to the two waves. The intensity at any point in this pattern depends on the phase as well as the amplitude of the original object wave. Accordingly, the processed photographic plate, which is called a hologram, contains information on both the amplitude and the phase of the object wave. However, since the hologram bears no resemblance to the object, this information is in a coded form.

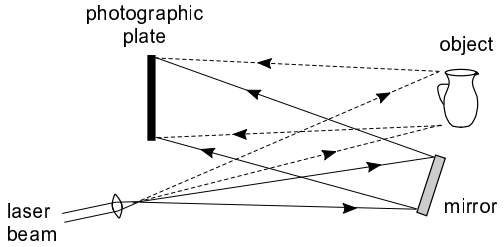

Figure 8.1: Recording a hologram. The photographic plate records the interference pattern produced by the light waves scattered from the object and a reference wave reflected to it by the mirror [90].

The reason for the success of holography is that the object wave can be regenerated from the hologram merely by illuminating it once again with the reference wave as shown in figure 8.2. To an observer, this reconstructed wave is indistinguishable from the original object wave; he sees a three-dimensional image which exhibits all the normal effects of perspective and depth of focus which the object would exhibit, if it were still there.

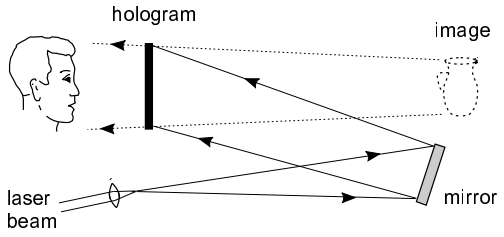

Figure 8.2: Reconstruction of the image. The hologram, after processing, is illuminated with the reference wave from the laser. Light diffracted by the hologram appears to come from the original object [90].

8.1 From Optical to Nuclear Holography

Holography was invented by Gabor in 1947 [91]. He presented a new principle to record in one diagram both the amplitude and the phase of a wavefield scattered by an object, and to reconstruct from this diagram the unknown object wavefield. This new idea was mainly applied to the optical domain. The recording and reconstruction were done using visible light. The real breakthrough came in the early 1960s with the advent of the laser which provided a powerful source of highly coherent light. Around the same time, the development of new techniques increased the image quality considerably [92, 93, 94, 95, 96, 97]. These advances set off an explosive growth in holography. However, nearly all applications remained in the domain of visible light. This limited the three-dimensional imaging to macroscopic objects of the orders of μm.

The increasing interest in microscopic objects (sizes of atoms or even smaller) stimulated the search for radiation sources of shorter wavelengths which could be used for holography with atomic resolution. In 1986 Szöke launched the idea of internal source holography [98]. He suggested that the individual atoms present in the sample could be used as sources of radiation. This idea was realized experimentally for the first time in 1990 using electrons as hologram-forming waves [99]. In the theoretical works of Refs. [100, 101] Barton, followed by Saldin, came to the conclusion that electron diffraction patterns could be reinterpreted as electron holograms. This opened a wide range of applications of electron holography. See, e.g., Refs. [102, 103, 104, 105, 106, 107, 108]. However, electron holography has the disadvantage that only surface layers can be viewed. To see into the bulk one needs deeply penetrating X-rays.

A theoretical comparison between electron and X-ray holography is presented in Ref. [109]. Both techniques yield three-dimensional information with atomic resolution. Due to the small cross-section for Thomson scattering, the holographic oscillations will be much weaker for X-ray than for electron scattering. This is confirmed in Ref. [110] where the possibility to use X-rays for holography with atomic resolution is analyzed. A holographic effect of $0.1 - 0.3\%$ is predicted. This value is much lower than for the case of electron holography where holographic oscillations in the range of $30 - 50\%$ of the reference wave are recorded. On the other hand, X-rays penetrate deep inside solids so that the three-dimensional information is not restricted to the surface.

The first internal source X-ray holograms were obtained in 1996 [111, 112, 113]. Two versions of X-ray holography were performed. In Ref. [111] direct X-ray fluorescence holography is reported. The sample is excited by an external X-ray beam. The excited atoms are the sources of the holo-

gram. When they deexcite, the emitted radiation can either go directly to a far-field detector (this is the holographic reference wave). Or, it can first be scattered on neighboring atoms before reaching the detector (the object wave). See figure 8.3 (left) for an illustration. The interference between both paths creates an intensity pattern as a function of the emission direction. In order to obtain atomic resolution, high Z elements should be used for which the K_α radiation has a sufficiently short wavelength.

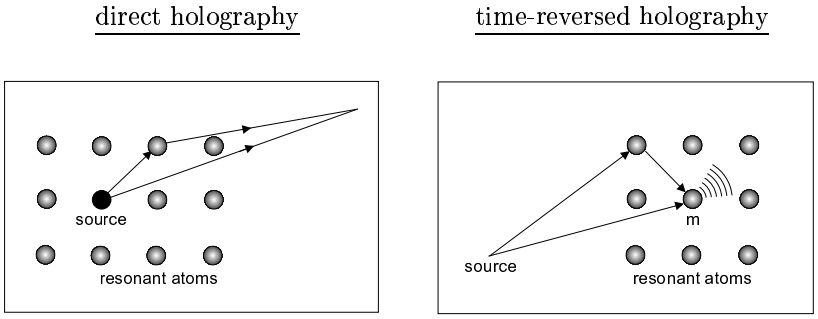

Figure 8.3: Two schemes for internal source holography.

In the second version, presented in Ref [113], a time-reversed picture is used. See figure 8.3 (right). Here, the positions of the source and the detector are interchanged. Radiation coming from an external source can reach a certain atom (detector) in the sample directly (reference wave) or indirectly, after it has been scattered by neighboring atoms (object wave). Again both fields interfere. If the total fluorescence of the detector atom is recorded as a function of the direction of the incident beam with respect to the sample, a holographic intensity pattern is obtained. This experiment is termed reversed X-ray fluorescence holography. It has the advantage that multiple-energy measurements are possible with strong tunable synchrotron sources. Multiple-energy holography has advantages for the reconstruction process, since the problems arising from twin images and self-interference effects can be overcome [114].

In X-ray holography, the radiation is scattered on electrons to form the holographic intensity pattern which contains information on the three-dimensional ordering of the atoms in the sample. One can also perform holography with γ-rays that are resonantly scattered by nuclei in the sample. This allows to obtain three-dimensional information on the nuclear environment. Again, two types of γ-ray holography can be distinguished: the direct one and the reversed one.

γ-ray holography using nuclear resonant scattering was for the first time successfully applied by Korecki [115] in the reversed version. In this experiment, an external ^{57}Co γ-ray source is used to excite nuclei in a thin epitaxial ^{57}Fe film. The radiation from the source can be absorbed directly by a detector nucleus, or after it has been resonantly scattered on neighboring nuclei. Both paths interfere, yielding fluctuations in the total number of conversion electrons emitted by the detector nucleus in the de-excitation process. The nuclear hologram is obtained by detecting the total conversion electron yield as a function of the incidence angle of the γ-rays. Holographic oscillations of 2% were measured and a spatial resolution in the reconstructed image of $0.7 - 3.1$ Å was reached.

In the other version, the direct γ-ray holography, the radioactive source atoms are located inside the sample itself. When a γ-ray is emitted, it can reach a far-field detector directly, or it can first be resonantly scattered on neighboring nuclei before reaching the detector. The interference between both paths creates a holographic intensity pattern as a function of the γ-ray direction.

The two versions of nuclear holography can be referred to as nuclear absorption holography and nuclear emission holography. Both use the concept of internal sources, but the latter in the direct version, the former in the reversed version.

In this part of the thesis, nuclear emission holography will be further investigated. First of all, a quantum mechanical theory is presented to describe the formation of a nuclear hologram. The results of the theory are further explored by means of simulations, which show the feasibility of a nuclear emission holography experiment. In chapter 11, a possible experiment is considered. Two candidate samples are discussed and an estimation for the data acquisition time is given. Finally, it is explained how to reconstruct from the hologram the real-space three-dimensional image of the nuclear environment. In a concluding chapter, the possible applications of nuclear emission holography are mentioned and the advantages and disadvantages compared to nuclear absorption holography are discussed.

Chapter 9

Quantum Mechanical Theory of the Formation of a Nuclear Emission Hologram

In the present chapter, the quantum mechanical theory describing the formation of a nuclear emission hologram is developed. The general method used to describe the interaction of photons and nuclei is taken from Heitler [116] and Harris [117]. It involves quantum mechanical calculations in frequency domain to obtain a set of coupled equations. These can be solved for the problem of an internal γ-ray source in the single-scattering approximation which is valid for small ensembles of resonant nuclei. The calculations yield a transparent formula for the radiated intensity as a function of the emission direction.

The theory presented here has been described in Ref. [118]. An outline of the theory will be given in this chapter. The complete calculations can be found in appendix B.

9.1 General Formalism

Consider the quantum mechanical system consisting of nuclei, photons and conversion electrons. The Hamiltonian of this system can be divided into two parts:

$$H = H_0 + V$$

H_0 is the unperturbed part which describes the evolution of the nuclear states, the free radiation field and the conversion electrons, in absence of any coupling. The perturbing part V describes the interaction of the three subsystems and is responsible for transitions between nuclear levels.

The eigenstates of the total Hamiltonian can be expressed as:

$$\mid \psi(t) > = \sum_l a_l(t)\, e^{-i\omega_l t} \mid \varphi_l(0) >$$

where $\mid \varphi_l(0) >$ is an eigenstate of H_0 belonging to the energy $\hbar\omega_l$.

Solving the Schrödinger equation

$$i\hbar \frac{d \mid \psi(t) >}{dt} = (H_0 + V) \mid \psi(t) >$$

leads to a set of coupled differential equations

$$i\hbar \frac{da_l(t)}{dt} = \sum_q a_q(t)\, e^{i(\omega_l - \omega_q)t} < \varphi_l(0) \mid V \mid \varphi_q(0) > \qquad (9.1)$$

A solution to this system is wanted that satisfies the condition that at $t = 0$ the system is in a well defined state, say n, and all other probability amplitudes are zero: $a_l(0) = 0$ and $a_n(+0) = 1$, where $t = +0$ means that t approaches zero from the positive side. Although a physically meaningful solution only involves positive times ($t \geq 0$), for analytical reasons the solution will be extended to the negative time axis.

We choose the a_l's such that $a_l(t) = a_n(t) = 0$ for $t < 0$. It then follows that a_n has a discontinuity that can be dealt with. In Ref. [116], it is shown that adding an extra term to the right-hand side of expression (9.1) takes care of the initial condition and the discontinuity.

$$i\hbar \frac{da_l(t)}{dt} = \sum_q a_q(t)\, e^{i(\omega_l - \omega_q)t} < \varphi_l(0) \mid V \mid \varphi_q(0) > + i\hbar\, \delta_{ln}\, \delta(t) \quad (9.2)$$

where δ_{ln} is the Kronecker delta and $\delta(t)$ the Dirac delta function.

For the further calculation, it is advantageous to express these equations in the frequency domain. Therefore, the following Fourier transforms are introduced [116]:

$$a_l(t) = -\frac{1}{2\pi i} \int_{-\infty}^{+\infty} d\omega\, A_l(\omega)\, e^{i(\omega_l - \omega)t}$$

$$i\,\delta(t) = -\frac{1}{2\pi i} \int_{-\infty}^{+\infty} d\omega\, e^{i(\omega_l - \omega)t}$$

Applying these transformations to the coupled differential equations (9.2) leads to the set

$$(\omega - \omega_l)\, A_l(\omega) = \sum_q A_q(\omega)\, \frac{V_{lq}}{\hbar} + \delta_{ln} \quad (9.3)$$

V_{lq} is the matrix element inducing a transition from the q^{th} unperturbed state to the l^{th} unperturbed state: $V_{lq} =< \varphi_l(0) \mid V \mid \varphi_q(0) >$.

To obtain an equation for $A_l(\omega)$, one would have to divide by $(\omega - \omega_l)$. This division will not be unique and it can be shown that if the a_l's are to fulfill the initial conditions, the result of the division by $(\omega - \omega_l)$ must be a factor $\lim_{\epsilon \downarrow 0} 1/(\omega - \omega_l + i\epsilon)$. This has only a mathematical meaning when integrals are involved, which eventually will be the case. In fact the replacement of $(\omega - \omega_l)$ by $(\omega - \omega_l + i\epsilon)$ where ϵ is an infinitesimal, positive number, defines the path of integration, guaranteeing causality [116]. Of course, the device $i\epsilon$ will always disappear from the physical answer, as will become clear later.

Thus, Eq. (9.3) can be rewritten as:

$$(\omega - \omega_l + i\epsilon)\, A_l(\omega) = \sum_q A_q(\omega)\, \frac{V_{lq}}{\hbar} + \delta_{ln} \quad (9.4)$$

The big advantage of applying the above Fourier transformation is the transition from a set of coupled differential equations to a set of linearly coupled algebraic equations, which are much easier to solve.

9.2 Fundamental Equations

The general formalism, introduced in the previous section, will now be applied to the problem of nuclear emission holography.

Consider a lattice of resonant nuclei, some of which are in the excited state (the source nuclei) and all the others are in the ground state (the scattering nuclei). The density of the source nuclei is assumed to be very low, so that the lattice can be divided into independent subsystems containing just one source nucleus surrounded by many scattering nuclei. In the following, the holographic image from one such a subsystem will be calculated. The image of the global lattice is obtained by summing the contributions of all independent subsystems.

As initial condition, suppose all scattering nuclei in the lattice are in the ground state and only one source nucleus, positioned at $\vec{r} = 0$, is excited. No photons or conversion electrons are present at $t = 0$. To keep the analysis as simple as possible, only one excited state with energy $\hbar\omega_0$ will be considered.
The following probability amplitudes are defined:

$A(\omega)$: the source nucleus is excited,
all scattering nuclei are in their ground state,
there are no photons
and no conversion electrons present

$B_m(\omega)$: the mth scattering nucleus at $\vec{r}_m$ is in its excited state,
all other nuclei are in their ground state,
there are no photons
and no conversion electrons present

$C_{\vec{k}}(\omega)$: all nuclei are in the ground state,
a photon of wave vector $\vec{k}$ is present,
there are no conversion electrons

$D_{\vec{p}}(\omega)$: all nuclei are in the ground state,
there are no photons,
a conversion electron with momentum $\vec{p}$, produced by the source nucleus, is present

$D_{m,\vec{p}}(\omega)$: all nuclei are in the ground state,
there are no photons,
a conversion electron with momentum $\vec{p}$, produced by the m^{th} scattering nucleus, is present

The coupled equations relating these amplitudes are the following:

$$(\omega - \omega_0 + i\epsilon)\ A(\omega) = \sum_{\vec{k}} \frac{V_{\vec{k}}}{\hbar}\ C_{\vec{k}}(\omega) + \sum_{\vec{p}} \frac{V_{\vec{p}}}{\hbar}\ D_{\vec{p}}(\omega) + 1 \tag{9.5}$$

$$\begin{aligned}(\omega - \omega_0 + i\epsilon)\ B_m(\omega) &= \sum_{\vec{k}} \frac{V_{\vec{k}}}{\hbar}\ e^{i\vec{k}\cdot\vec{r}_m}\ C_{\vec{k}}(\omega) \\ &+ \sum_{\vec{p}} \frac{V_{\vec{p}}}{\hbar}\ e^{i\vec{p}\cdot\vec{r}_m/\hbar}\ D_{m,\vec{p}}(\omega)\end{aligned} \tag{9.6}$$

$$(\omega - \omega_{\vec{k}} + i\epsilon)\ C_{\vec{k}}(\omega) = \frac{V^*_{\vec{k}}}{\hbar}\ A(\omega) + \sum_m \frac{V^*_{\vec{k}}}{\hbar}\ e^{-i\vec{k}\cdot\vec{r}_m}\ B_m(\omega) \tag{9.7}$$

$$(\omega - \omega_{\vec{p}} + i\epsilon)\ D_{\vec{p}}(\omega) = \frac{V^*_{\vec{p}}}{\hbar}\ A(\omega) \tag{9.8}$$

$$(\omega - \omega_{\vec{p}} + i\epsilon)\ D_{m,\vec{p}}(\omega) = \frac{V^*_{\vec{p}}}{\hbar}\ e^{-i\vec{p}\cdot\vec{r}_m/\hbar}\ B_m(\omega) \tag{9.9}$$

Here $V_{\vec{k}}$ and $V^*_{\vec{k}}$ are the matrix elements describing absorption and emission of a photon with wave vector $\vec{k}$, respectively. Analogously, the matrix elements $V_{\vec{p}}$ and $V^*_{\vec{p}}$, describe absorption or emission of a conversion electron with momentum $\vec{p}$.

The structure of these equations can be understood as follows:

- Eq. (9.5) expresses the amplitude for finding the source nucleus in an excited state (left-hand side). This state can be obtained by absorption of a photon by the source nucleus (first term on the right-hand side), by absorption of a conversion electron coming from the source (second term on the right-hand side), or by the initial excitation at $t = 0$ (the constant term 1).
- A similar interpretation holds for Eq. (9.6). The m^{th} scattering nucleus can be excited by absorption of a photon (first term on the right-hand side) or by absorption of its own conversion electron (second term). The phase factors $e^{i\vec{k}\cdot\vec{r}_m}$ and $e^{i\vec{p}\cdot\vec{r}_m/\hbar}$ are introduced in order to specify the location where the absorption process occurred.
- Eq. (9.7) gives the amplitude for having a photon with wave vector $\vec{k}$ present. This photon can be emitted by the source nucleus (first term on the right-hand side) or by the other nuclei (second term). The phase factor $e^{-i\vec{k}\cdot\vec{r}_m}$ again accounts for the position where the emission took place.

- Eq. (9.8) states that a conversion electron from the source can only originate by emission of the electron by the source nucleus.
- Similarly, in Eq. (9.9), a conversion electron from the m^{th} scattering nucleus can only be present after the emission of the electron by the m^{th} scattering nucleus.

It should be emphasized at this stage that the treatment of the electron conversion processes is only necessary to produce a width (and also a shift that will be incorporated into ω_0) due to electron conversion. This can be verified from the detailed calculation given in appendix B.

By combining Eqs. (9.5) - (9.9), the fundamental equations describing the system can be shown to be (see appendix B.1):

$$(\omega - \omega_0 + i\,\frac{\Gamma}{2\hbar})\,A(\omega) \;=\; 1 + \sum_m \sum_{\vec{k}} \frac{|V_{\vec{k}}|^2}{\hbar^2}\,\frac{e^{-i\vec{k}\cdot\vec{r}_m}}{\omega - \omega_{\vec{k}} + i\epsilon}\,B_m(\omega) \qquad (9.10)$$

$$\begin{aligned}(\omega - \omega_0 + i\,\frac{\Gamma}{2\hbar})\,B_m(\omega) \;&=\; \sum_{\vec{k}} \frac{|V_{\vec{k}}|^2}{\hbar^2}\,\frac{e^{i\vec{k}\cdot\vec{r}_m}}{\omega - \omega_{\vec{k}} + i\epsilon}\,A(\omega) \\ &+\; \sum_{m'\neq m} \sum_{\vec{k}} \frac{|V_{\vec{k}}|^2}{\hbar^2}\,\frac{e^{i\vec{k}\cdot(\vec{r}_m - \vec{r}_{m'})}}{\omega - \omega_{\vec{k}} + i\epsilon}\,B_{m'}(\omega) \qquad (9.11)\end{aligned}$$

$$(\omega - \omega_{\vec{k}} + i\epsilon)\,C_{\vec{k}}(\omega) \;=\; \frac{V^*_{\vec{k}}}{\hbar}\,A(\omega) + \sum_m \frac{V^*_{\vec{k}}}{\hbar}\,e^{-i\vec{k}\cdot\vec{r}_m}\,B_m(\omega) \qquad (9.12)$$

where Γ is the total linewidth of the excited state, given by the sum of the conversion electron width γ_C and the radiative width γ_R.

Eqs. (9.10)-(9.12) describe the interaction of electromagnetic radiation with a nuclear system. The positions of all resonant nuclei occur in the expressions via the factors $e^{\pm i\vec{k}\cdot\vec{r}_m}$.

This set of linearly coupled equations has been solved exactly in the case of radiation coming from a radioactive source, scattered in the forward direction [63, 119] and in the case of nuclear forward scattering of synchrotron radiation [15]. For nuclear emission holography, an analytical solution can only be obtained when certain assumptions are made.

9.3 Approximate Solution

The set of fundamental equations (9.10)-(9.12) can be solved analytically in the single-scattering approximation, in which the following two hypotheses are assumed:

1. The probability of reexcitation of the source nucleus by radiation coming from the surrounding nuclei is negligible. Therefore, this process will be excluded. This is justified for interatomic distances > 1 Å, which is always the case.
2. Only single scattering by the scattering nuclei is considered. This is an excellent approximation for thin samples.

The sums over m and $\vec{k}$ on the right-hand side of Eq. (9.10) describe absorption by the source nucleus of radiation coming from the scattering nuclei. According to hypothesis (1), this process will be neglected. Therefore,

$$A(\omega) = \frac{1}{\omega - \omega_0 + i\Gamma/2\hbar} \tag{9.13}$$

This is nothing but the familiar Lorentzian frequency spectrum, centered about ω_0 with a full width at half maximum of $\Gamma/\hbar$.

The last series on the right-hand side of Eq. (9.11) describes the excitation of the scattering nucleus at position $\vec{r}_m$ due to radiation coming from the other scattering nuclei. These processes are neglected according to hypothesis (2). Thus,

$$\left(\omega - \omega_0 + i\frac{\Gamma}{2\hbar}\right) B_m(\omega) = \sum_{\vec{k}} \frac{|V_{\vec{k}}|^2}{\hbar^2} \frac{e^{i\vec{k}\cdot\vec{r}_m}}{\omega - \omega_{\vec{k}} + i\epsilon} A(\omega) \tag{9.14}$$

Using Eqs. (9.12), (9.13) and (9.14), an expression for $C_{\vec{k}}(\omega)$ can be calculated. For the details of the calculation, the reader is referred to appendix B.2. The result is:

$$\begin{aligned} C_{\vec{k}}(\omega) &= \frac{V_{\vec{k}}^*}{\hbar} \frac{1}{\omega - \omega_0 + i\Gamma/2\hbar} \frac{1}{\omega - \omega_{\vec{k}} + i\epsilon} \\ &- \frac{V_{\vec{k}}^*}{\hbar} \frac{\gamma_R}{2\hbar} \frac{1}{(\omega - \omega_0 + i\Gamma/2\hbar)^2} \frac{1}{\omega - \omega_{\vec{k}} + i\epsilon} \sum_m \frac{e^{i\omega r_m/c}}{\omega r_m/c} e^{-i\vec{k}\cdot\vec{r}_m} \end{aligned} \tag{9.15}$$

Fourier transforming this expression back to time domain, one obtains (cf. appendix B.3)

$$c_{\vec{k}}(t) = c_{\vec{k}}^{(0)}(t) + c_{\vec{k}}^{(1)}(t)$$

with

$$c_{\vec{k}}^{(0)}(t) = \frac{V_{\vec{k}}^*}{\hbar} \frac{1}{\omega_{\vec{k}} - \omega_0 + i\Gamma/2\hbar} \left[1 - e^{i(\omega_{\vec{k}} - \omega_0 + i\Gamma/2\hbar)t}\right] \tag{9.16}$$

$$\begin{aligned} c_{\vec{k}}^{(1)}(t) = & -\frac{V_{\vec{k}}^*}{2\hbar^2} \frac{\gamma_R}{(\omega_{\vec{k}} - \omega_0 + i\Gamma/2\hbar)^2} \sum_m e^{-i\vec{k}\cdot\vec{r}_m} \frac{e^{i\omega_{\vec{k}} r_m/c}}{\omega_0 r_m/c} \\ & \times \Big\{1 + i(\omega_{\vec{k}} - \omega_0 + i\Gamma/2\hbar)(t - r_m/c)\, e^{i(\omega_{\vec{k}} - \omega_0 + i\Gamma/2\hbar)(t - r_m/c)} \\ & - e^{i(\omega_{\vec{k}} - \omega_0 + i\Gamma/2\hbar)(t - r_m/c)}\Big\} \end{aligned} \tag{9.17}$$

The probability of having a photon with wave vector $\vec{k}$ present at time t, is given by

$$\begin{aligned} I_{\vec{k}}(t) &= \left|c_{\vec{k}}(t)\right|^2 \\ &= \left|c_{\vec{k}}^{(0)}(t)\right|^2 + \left|c_{\vec{k}}^{(1)}(t)\right|^2 + 2\, Re\, [c_{\vec{k}}^{(0)}(t)\, c_{\vec{k}}^{(1)*}(t)] \\ &= I_{\vec{k}}^{00}(t) + I_{\vec{k}}^{11}(t) + I_{\vec{k}}^{01}(t) \end{aligned}$$

If one considers the probability that a photon has been emitted in the direction $\vec{k}$ for long times ($t \to \infty$), the previous expression should be evaluated in the limit $t \to \infty$

$$I_{\vec{k}}(\infty) = \lim_{t\to\infty} \left|c_{\vec{k}}(t)\right|^2$$

This yields the following formula

$$I_{\vec{k}}(\infty) = \underbrace{\frac{|V_{\vec{k}}|^2}{\hbar^2} \frac{1}{(\omega_{\vec{k}} - \omega_0)^2 + (\Gamma/2\hbar)^2}}_{I_{\vec{k}}^{00}(\infty)}$$

$$+ \underbrace{\frac{|V_{\vec{k}}|^2 \gamma_R^2}{4\hbar^4} \frac{1}{[(\omega_{\vec{k}} - \omega_0)^2 + (\Gamma/2\hbar)^2]^2} \sum_m \sum_{m'} \frac{e^{i\vec{k}\cdot(\vec{r}_m - \vec{r}_{m'})}}{\omega_0 r_m/c} \frac{e^{-i\omega_{\vec{k}}(r_m - r_{m'})/c}}{\omega_0 r_{m'}/c}}_{I_{\vec{k}}^{11}(\infty)}$$

$$\underbrace{-Re\{ \frac{|V_{\vec{k}}|^2 \gamma_R}{\hbar^3} \frac{1}{(\omega_{\vec{k}} - \omega_0)^2 + (\Gamma/2\hbar)^2} \frac{1}{\omega_{\vec{k}} - \omega_0 - i\Gamma/2\hbar} \sum_m e^{i\vec{k}\cdot\vec{r}_m} \frac{e^{-i\omega_{\vec{k}} r_m/c}}{\omega_0 r_m/c} \}}_{I_{\vec{k}}^{01}(\infty)}$$

The above equation can be divided into three parts:

- The first term, $I_{\vec{k}}^{00}(\infty)$, is the probability to have a photon with wave vector $\vec{k}$, due to the presence of the source nucleus alone. This term contains no information on the positions of the surrounding nuclei. It just gives the frequency distribution of the radiation emitted by the source.
- The second term, $I_{\vec{k}}^{11}(\infty)$, is the probability to have a photon with wave vector $\vec{k}$, due to the presence of the scattering nuclei having scattered the photon produced by the source nucleus. This term depends on the positions $\vec{r}_m$ of all nuclei with respect to the source.
- The last term on the right-hand side, $I_{\vec{k}}^{01}(\infty)$, is an interference term between the amplitude due to the source nucleus and all amplitudes due to the scattering nuclei.

It is clear that the counting rate depends on the direction of detection via the factors $e^{i\vec{k}\cdot\vec{r}_m}$, and also on the energy $\hbar\omega_{\vec{k}}$ of the detected radiation. However, the detector, positioned in a certain direction, does not register a single energy. Thus, one has to integrate the intensity over all energy values. When doing so, the intensity will depend solely on the direction, represented by the unit vector $\hat{k} = \vec{k}/\mid \vec{k} \mid$.

The recorded intensity becomes (see appendix B.4):

$$I(\hat{k}) = I^{00}(\hat{k}) + I^{01}(\hat{k}) + I^{11}(\hat{k})$$

with

$$I^{00}(\hat{k}) = \frac{|V(\omega_0)|^2 \, L}{\Gamma \hbar c} \tag{9.18}$$

$$I^{01}(\hat{k}) = -\frac{|V(\omega_0)|^2 \, L}{\Gamma \hbar c} \frac{\gamma_R}{\Gamma} \sum_m \frac{\sin[(1 - \hat{k} \cdot \hat{r}_m) \, \omega_0 \, r_m / c]}{\omega_0 \, r_m / c} \tag{9.19}$$

$$I^{11}(\hat{k}) = \frac{1}{2} \frac{|V(\omega_0)|^2 \, L}{\Gamma \hbar c} \frac{\gamma_R^2}{\Gamma^2} \times \sum_m \sum_{m'} \frac{\cos\left[\left((1 - \hat{k} \cdot \hat{r}_m) \, r_m - (1 - \hat{k} \cdot \hat{r}_{m'}) \, r_{m'}\right) \, \omega_0 / c\right]}{\omega_0 \, r_m / c \qquad \omega_0 \, r_{m'} / c} \tag{9.20}$$

The length L appearing in these equations comes from the conversion of a sum over all energies into an integral.

Measuring the intensity as a function of the emission direction will give a nuclear emission hologram. Holographic oscillations, given by $I^{01}(\hat{k}) + I^{11}(\hat{k})$, are superposed on a constant background, due to $I^{00}(\hat{k})$. They contain all information on the positions of the scattering nuclei with respect to the source nucleus.

Remark

In the calculations above, electronic absorption has been neglected. This is justified because typical electronic absorption lengths for γ-rays are in the order of μm, while the dimensions of the nuclear ensembles that will be considered for nuclear emission holography will be in the range of several nm.

Chapter 10

Holographic Image

A nuclear emission hologram is obtained when the intensity of γ-rays emitted by internal sources is recorded as a function of the emission direction. The resulting intensity pattern is composed of a constant background due to the radiation coming directly from the source, and holographic oscillations. These oscillations can be separated from the hologram by defining a contrast function. Using the results obtained in the previous chapter, an explicit expression for the contrast function is derived for the case of a single-line sample. The properties of the contrast function are explored by means of simulations. They show a holographic effect of the order of a few percent.

The hologram contains information on all resonant nuclei in the sample. However, in applications of nuclear holography the interest goes to the direct environment of the source nucleus. Nuclei situated far away will give a high-frequency contribution to the contrast function. In section 10.3 it will be shown that this contribution can be eliminated from the hologram by applying a Fourier filtering procedure.

Finally, the validity of the single-scattering approximation in nuclear emission holography is discussed.

10.1 Contrast Function

The hologram is created by interference of a known reference wave with an unknown object wave. From the resulting intensity pattern $I(\hat{k})$ a normalized hologram function $F(\hat{k})$ can be calculated by removing the reference wave and normalizing the expression. With the notations of the previous chapter, one has

$$F(\hat{k}) = \frac{I(\hat{k}) - I^{00}(\hat{k})}{I^{00}(\hat{k})}$$

Or,

$$F(\hat{k}) = \frac{I^{01}(\hat{k})}{I^{00}(\hat{k})} + \frac{I^{11}(\hat{k})}{I^{00}(\hat{k})} \tag{10.1}$$

This function merely contains the holographic oscillations and, therefore, will be called the contrast function.

For a small number of scattering nuclei, $I^{11}(\hat{k})$ is much smaller than $I^{01}(\hat{k})$ so that the second term in Eq. (10.1) can be neglected. This, however, is only justified for small structures with a limited amount of resonant nuclei. As can be seen from Eq. (9.20), if the number of scattering nuclei increases, $I^{11}(\hat{k})$ becomes comparable to or even larger than $I^{01}(\hat{k})$; this because of the additional summation $\sum_{m'}$. In that case $I^{11}(\hat{k})$ can no longer be neglected and the full expression for the contrast function should be used.

In the following, only small samples will be considered for which the contrast function can be approximated by

$$F(\hat{k}) \approx \frac{I^{01}(\hat{k})}{I^{00}(\hat{k})}$$

Using Eqs. (9.18) and (9.19) from chapter 9, an explicit expression for the contrast function in nuclear emission holography is derived in the single-scattering approximation and assuming no hyperfine interactions:

$$F(\hat{k}) = -\frac{\gamma_R}{\Gamma} \sum_m \frac{sin\left[(1 - \hat{k} \cdot \hat{r}_m)\, \omega_0 r_m / c\right]}{\omega_0 r_m / c} \tag{10.2}$$

10.1.1 Properties of the Contrast Function

The contrast function $F(\hat{k})$ depends on the direction $\hat{k}$ with respect to the positions $\vec{r}_m$ of the scattering nuclei. Knowledge of $F(\hat{k})$ thus will give information on the positions of these nuclei with respect to the source.

Each resonant nucleus gives a contribution to the contrast function. From Eq. (10.2), it follows that the further away the scattering nucleus is located, the smaller the amplitude of the oscillations and the higher the oscillation frequency are. These two features are illustrated in figure 10.1

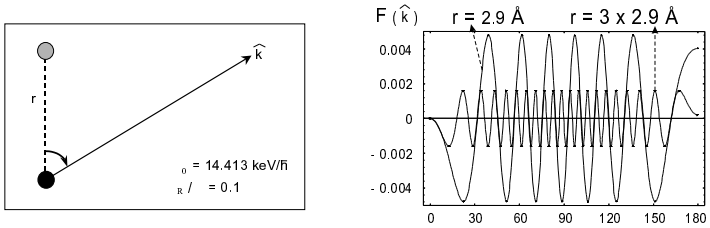

Figure 10.1: Simulation of the contrast function for two ^{57}Fe nuclei: the scattering nucleus (gray) is positioned at 2 different distances from the source nucleus (black). Left: geometry. Right: contrast function for 2 inter-nuclear distances.

In the case of only one scattering nucleus, the intensity pattern of the emitted radiation will be axially symmetric about the direction source-scatterer. The contrast function can therefore be characterized by only one parameter θ (see figure 10.1). In general, however, the contrast function will depend on the two spherical angular coordinates θ and φ.

As can be seen from figure 10.1, each component of the contrast function oscillates with changing frequency, resulting in a series of nonequidistant maxima and minima. For the simple case of only one scattering nucleus, located at 2.9 Å from the source, the angular distance between a maximum and its adjacent minimum is about 8° for radiation emitted in the vicinity of 90°. For smaller or larger angles, this angular distance increases. For example, a maximum occurs around 37° and its adjacent minimum around 20°.

The contrast, defined as the difference between the maximum and the minimum of the normalized intensity, will be determined by the configuration. For a ^{57}Fe ensemble containing only one scattering nucleus positioned at 2.9 Å from the source, the contrast is approximately 1%. This value increases if the distance source-scatterer decreases, or, if the number of resonant nuclei surrounding the source increases.

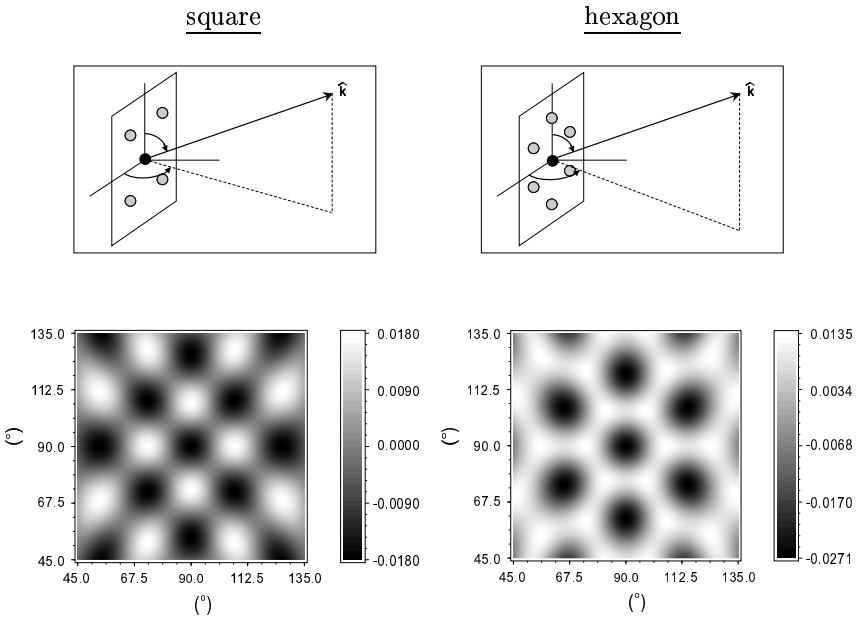

Figure 10.2: Simulation of the contrast function for an ensemble of ^{57}Fe nuclei: the scattering nuclei (gray) are positioned at $\frac{\sqrt{2}}{2} \times 2.9$ Å from the source nucleus (black) at the corners of a square (left) or at the corners of a regular hexagon (right). Top: geometry. Bottom: contrast function.

In figure 10.2 the normalized holographic image is shown for two different configurations. In the first simulation, the source is surrounded by four scattering nuclei on the corners of a square. In the second simulation, six scattering nuclei are located on the corners of a regular hexagon. The distance source-scatterer is fixed to $\frac{\sqrt{2}}{2} \times 2.9$ Å.

The contrast functions look very different. They exhibit the symmetry of the nuclear ensemble. In the first case a four-fold symmetry can be recognized in the holographic image, while for the hexagon, a six-fold symmetry is clearly observed.

Figure 10.3 shows similar simulations, for three-dimensional structures. On the left, the contrast function for a cubic unit cell with 8 scattering nuclei is shown. On the right, the contrast function is displayed for 12 scattering nuclei on the corners of a simple hexagonal structure (see configuration on top of figure 10.3). The source nucleus is positioned in the center of the cell, at $\frac{\sqrt{3}}{2} \times 2.9$ Å from all scattering nuclei. Again, cubic or hexagonal symmetry is recognized.

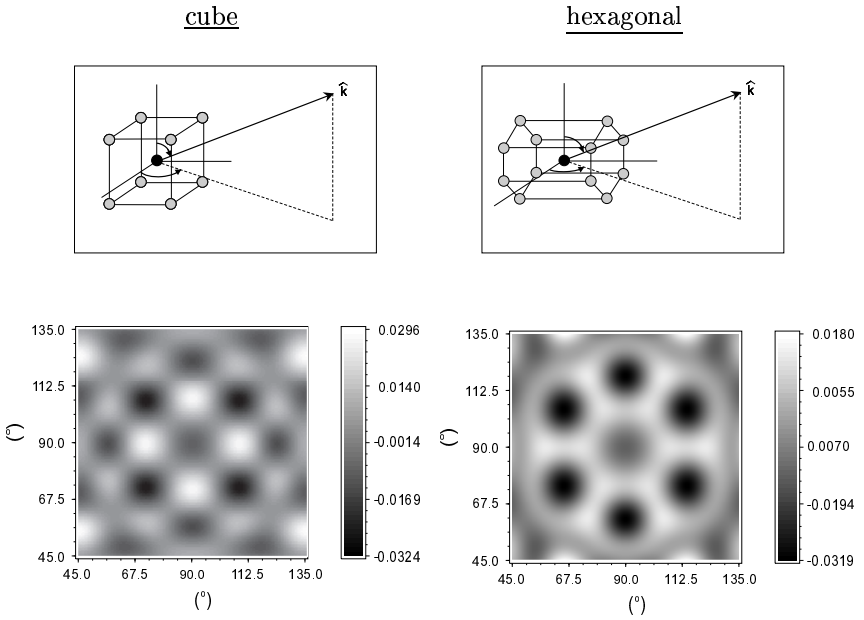

Figure 10.3: Simulation of the contrast function for an ensemble of ^{57}Fe nuclei: the scattering nuclei (gray) are positioned at $\frac{\sqrt{3}}{2} \times 2.9$ Å from the source nucleus (black). Left: the resonant nuclei form a cubic cell with dimension 2.9 Å. Right: the resonant nuclei form a simple hexagonal cell, given by the parameters 2.9 Å (longitudinal distance along the c-axis) and $\sqrt{2} \times 2.9$ Å (lateral distance perpendicular to the c-axis). Top: geometry. Bottom: contrast function.

The previous simulations show that the normalized holographic image is characteristic for a particular configuration. It contains all information on the position of the resonant nuclei with respect to the source. From the intensity pattern, the three-dimensional real space image can be reconstructed according to certain techniques. This will be explained in chapter 11.

10.2 Simulations for a Bcc Lattice of ^{57}Fe

In the following a bcc lattice of ^{57}Fe will be considered. The source is a ^{57}Fe nucleus in its first excited state, located at a substitutional lattice site. The other sites are occupied by resonant ^{57}Fe nuclei in the ground state.

Figure 10.4 shows the simulated contrast function for a bcc lattice of ^{57}Fe. The source nucleus is located at the origin of the coordinate system. The intensity is shown as a function of the spherical angular coordinates θ and φ as they were defined in figure 10.3 (top, left). The contrast function is displayed, taking into account only scattering nuclei within a certain radius around the source. Due to the cubic symmetry of the bcc lattice, the intensity pattern corresponding to $45° \leq \theta, \varphi \leq 135°$ is repeated periodically in all directions. Therefore, only this part of the hologram is displayed.

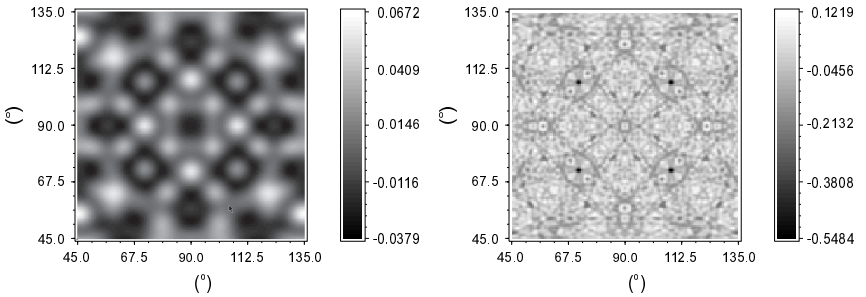

Figure 10.4: Simulations of the contrast function for a bcc lattice of ^{57}Fe. Left: only contributions from scattering nuclei within 2 a_0 (64 nearest neighbors) are taken into account. Right: contributions from scattering nuclei within 10 a_0 (8392 neighbors) are taken into account.

In the first simulation (on the left) resonant nuclei within a radius of two times the lattice constant ($a_0 = 2.866$ Å) are considered. This means only contributions of the 64 nearest neighbors of the source are taken into account. This gives a very clear normalized hologram.
If the radius of scattering nuclei is increased to 10 a_0, the contrast function looks like the picture on the right. This intensity pattern is much more detailed, exhibiting faster oscillations due to contributions of nuclei situated further away. Each far-away nucleus individually gives only a very small contribution to the contrast function (the amplitude is substantially decreased). But the large number of them makes that the total signal from nuclei far-away is large. The fast oscillations will mask the information on the direct environment of the source. It will be explained how these high-frequency contributions can be filtered out of the holographic image.

10.3 Low-pass Filtering

A low-pass filter should suppress the high-frequency contributions to the signal, while leaving the low-frequency contributions unchanged.

The Fourier transformed signal should be multiplied with a function being one for low-frequency values and zero for high-frequency values. Two filter functions will be considered:
The step function:

$$\begin{aligned} s(x) &= 1 && \text{if } -x_0 \leq x \leq x_0 \\ &= 0 && \text{else} \end{aligned}$$

and the Gaussian:

$$g(x) = e^{-x^2/2x_0^2}$$

The main difference between both filter functions is that the first one eliminates the high frequencies completely, whereas the Gaussian only reduces their contribution. The component with frequency x_0 is reduced by the Gaussian filter to 61%, the $2 \times x_0$ component is reduced to 14%, etc. At first sight, this argument would lead to a choice in favor of the step function. But, as will be shown below, the Gaussian has some important advantages over the step function that make it the most appropriate filter function for a nuclear emission hologram.

When applying the low-pass filter to the signal itself, the hologram should be convoluted with the inverse Fourier transformations of the filter functions.
For the step function this yields:

$$S(k_x) = \frac{\sin(x_0 k_x)}{\pi k_x}$$

The inverse Fourier transformation of a Gaussian is again a Gaussian:

$$G(k_x) = \frac{e^{-k_x^2/2\sigma^2}}{\sqrt{2\pi}\,\sigma} \qquad \text{with } \sigma = 1/x_0 \tag{10.3}$$

Figure 10.5 shows both functions in Fourier and in real space. The Gaussian as a function of k_x approaches zero much faster than the transformed step function. This has two consequences:

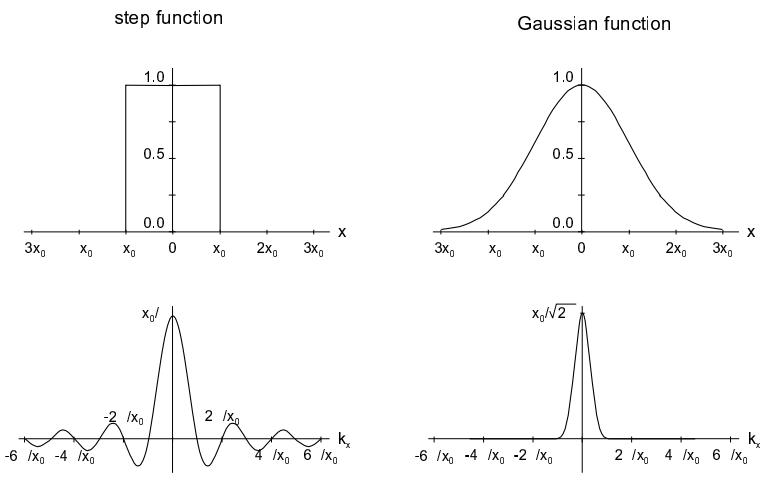

Figure 10.5: Two low-pass filters: The step function (left) and the Gaussian function (right). The functions are shown in Fourier and in real space.

- First of all, the Gaussian filter will introduce less border effects. If the holographic signal is not recorded over the full sphere, the filtering will give inaccurate results at the borders. The filtered signal at a particular point in the hologram is calculated by means of the signal values in the neighborhood of this point. When the holographic signal is not recorded over the complete sphere, it will be extended with noughts. As a result, the values of the filtered signal will be incorrect at the borders of the hologram. This problem is not encountered when a full holographic period is recorded. E.g., in case of a ^{57}Fe bcc lattice, if the contrast functions is known for $45° \leq \theta \leq 135°$ and $45° \leq \varphi \leq 135°$, the signal can be repeated periodically and the filtering will give correct results for all points in the hologram.

- Secondly, as mentioned before, the oscillation frequencies are not constant. They are the lowest near $\theta = 0°$ and get larger as θ approaches the value of 90°. This, of course, will have its repercussions on the filtering. For the signal coming from nuclei far-away from the source, there will be a region where the oscillations are much slower and thus are not correctly filtered. The faster the filter function goes to zero, the less sensitive it is to variations in oscillation frequency. Again, the Gaussian filter has the best performance.

10.3.1 Filtering Procedure

The holographic signal can be filtered by convoluting the contrast function $F(k_x, k_y)$ with a two-dimensional Gaussian function. The filtered image $H(k'_x, k'_y)$ is obtained by:

$$H(k'_x, k'_y) = \int_{-\infty}^{+\infty} dk_x \int_{-\infty}^{+\infty} dk_y \; F(k_x, k_y)\, G(k_x - k'_x)\, G(k_y - k'_y)$$

where G is the Gaussian function given by Eq. (10.3).

In Ref. [120] it has been explained how this formula should be adapted when the contrast function is parameterized by the spherical angular coordinates θ and φ. The result is:

$$H(\theta_0, \varphi_0) = \frac{1}{N} \int_0^{2\pi} d\varphi \int_0^{\pi} d\theta \, \sin\theta \; F(\theta, \varphi)\, e^{-\theta'^2/2\sigma^2} \tag{10.4}$$

with θ' defined by

$$\cos\theta' = \cos\theta_0 \; \cos\theta + \sin\theta_0 \; \sin\theta \; \cos(\varphi - \varphi_0)$$

The normalization factor N is given by

$$N = \int_0^{2\pi} d\varphi \int_0^{\pi} d\theta \, \sin\theta \; e^{-\theta^2/2\sigma^2}$$

For small values of σ ($\sigma \leq 0.140$), $N \approx 2\,\pi\,\sigma^2$ and $e^{-\theta'^2/2\sigma^2} \approx e^{(\cos\theta' - 1)/\sigma^2}$. So that Eq. (10.4) becomes

$$\begin{aligned} H(\theta_0, \varphi_0) \;\approx\; & \frac{1}{2\pi\sigma^2} \int_0^{2\pi} d\varphi \int_0^{\pi} d\theta \, \sin\theta \; F(\theta, \varphi)\, e^{\cos\theta_0 \cos\theta/\sigma^2} \\ & \times e^{(\sin\theta_0 \sin\theta \; \cos(\varphi - \varphi_0) \, - \, 1)/\sigma^2} \end{aligned}$$

The width σ determines the frequencies that will be maintained in the filtered signal and to what extent the high frequencies are reduced. The optimal width can be obtained by comparing the filtered hologram with the intensity pattern obtained from the close environment of the source.

10.3.2 Applying Low-pass Filtering to Simulations

For the bcc lattice of ^{57}Fe nuclei, the low-pass filter has been applied to the contrast function obtained for resonant nuclei within a radius of 10 a_0 from the source (see figure 10.7, top right). The filtered hologram is compared to the contrast function for resonant nuclei within a radius of 2 a_0 (figure 10.7, top left). Figure 10.6 shows the mean quadratic deviation for several values of σ. A minimum is observed for $\sigma = 3.3°$.

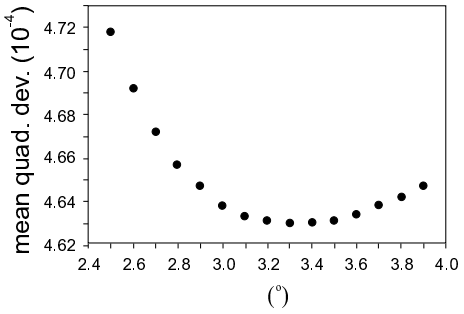

Figure 10.6: Mean quadratic deviation between the filtered image from figure 10.7 (top right) and the (unfiltered) image from figure 10.7 (top left) as a function of the Gaussian width σ. In order to avoid inaccuracies due to border effects, the mean quadratic deviation is calculated for $60° < \theta < 120°$ and $64° < \varphi < 115°$.

In the lower half of figure 10.7 the normalized holographic images after filtering with a two-dimensional Gaussian ($\sigma = 3.3°$) are displayed. When the filter is applied to the image of the large environment of the source (radius = 10 a_0), the fast oscillations disappear and a nice picture is obtained that looks very much like figure 10.7 (top left) for only the 64 nearest neighbors of the source. Applying the same filter to the image for the close environment of the source (radius = 2 a_0) has only very little effect. The intensity scale is slightly shifted and the amplitude of the holographic oscillations has been reduced. Where the effect before filtering was $\approx 10.5\%$, after filtering it is decreased to $\approx 5.5\%$.

A close look to the filtered images and the unfiltered one for the small ensemble reveals some directions that are incorrectly processed (e.g., $\theta = \varphi = 72°$). These points correspond to directions with a higher density of resonant nuclei. In the direction of a scattering nucleus the oscillation frequency as a function of $\hat{k}$ is at its minimum. As a consequence, the filtering procedure will not work properly in this direction. When there are many far-away nuclei in a certain direction, the filtering errors add and a

large deviation from the simulation for the close environment is observed. This fact may also be responsible for the change of the intensity scale.

The simulations below show that the image from the close environment of the source is hidden in the holographic intensity pattern obtained from a larger ensemble of scattering nuclei. By applying an appropriate low-pass Gaussian filter it is possible to extract the underlying information of the local surrounding of the source.

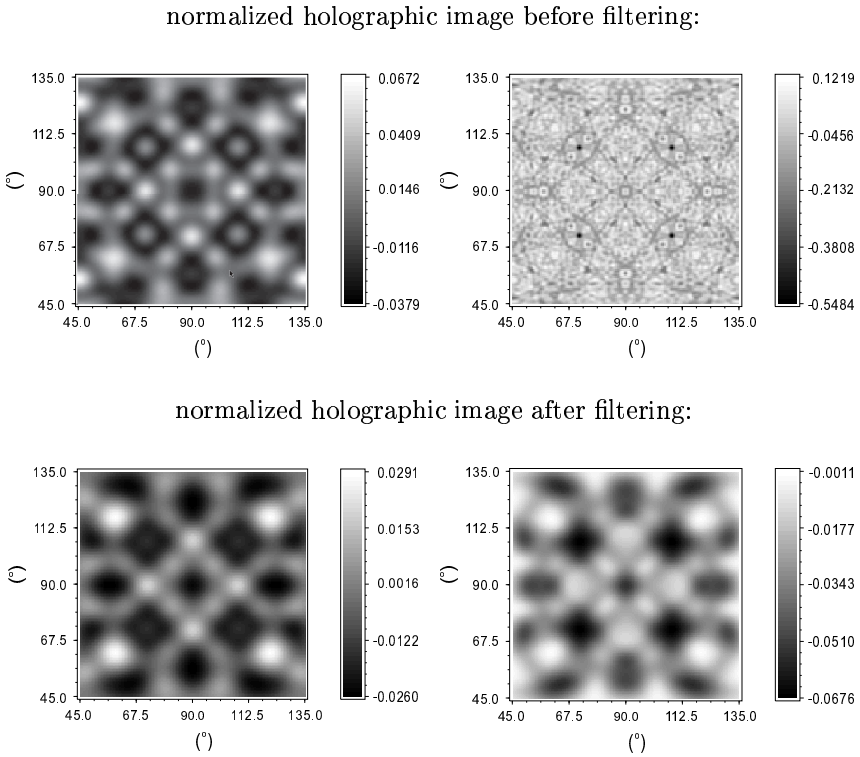

Figure 10.7: Simulations of the contrast function for a bcc lattice of ^{57}Fe. Left: only contributions from scattering nuclei within a radius of 2 a_0 from the source nucleus are taken into account. Right: contributions from scattering nuclei within a radius of 10 a_0. Below, the same holographic images are shown after filtering with a two-dimensional Gaussian ($\sigma = 3.3°$).

10.4 Discussion

An expression for the contrast function in the case of a single-line sample has been derived. In this expression, the self-interference term arising from interferences between two object waves has been neglected. This is justified for small ensembles of scattering nuclei ($10^3 - 10^4$ resonant nuclei). However, the approximation is no longer valid for nearly perfect single crystals where long-range coherence effects become important. In that case, the single-scattering approximation, used in the previous chapter to describe nuclear emission holography, does no longer hold and should be replaced by the dynamical theory for emission of Mössbauer γ-rays from crystals [121, 122].

A consequence of the long-range translational periodicity in single crystals is the appearance of Kossel lines [123]. Kossel lines are formed if a source of short wavelength radiation ($\approx$ 1 Å) is located inside a crystal on a crystallographic site. They are analogous to the well known Bragg peaks in traditional crystallography, except that in the Bragg case there is an external source and in the Kossel case there is an internal source. Directions satisfying Bragg's law lie on so-called Kossel cones with their axes perpendicular to the diffraction planes and with opening half-angles equal to $90° - \theta_B$, θ_B being the Bragg angle. Intersections of the Kossel cones with the hologram give a set of light and dark lines which distort the holographic image significantly [124]. Since the Kossel line pattern originates from the long-range periodicity and, hence, involves nuclei that are at large distances from the source, it can be eliminated by a low-pass filter which suppresses the contributions of distant nuclei.

The γ-radiation emitted by the source nucleus will not only scatter on neighboring nuclei, but also on the surrounding atoms. The Thomson scattering on electrons will give rise to another holographic intensity pattern. In case of enriched samples, the Thomson hologram will be much weaker than the nuclear hologram as can be seen from the simulations in Ref. [125]. The total cross-section for Thomson scattering [46] and for nuclear resonant scattering [13] are given, respectively, by

$$\sigma_{\text{Thomson}} = \frac{8\pi}{3} Z r_e^2$$

$$\sigma_{\text{nuclear}} = \frac{2\pi}{k^2} \frac{\gamma_R}{\Gamma} \frac{2j_e + 1}{2j_g + 1}$$

$r_e = 2.817 \cdot 10^{-13}$ cm is the classical electron radius, Z is the atomic number, j_g and j_e are the spins of the nuclear ground and excited states

and $k = 2\pi/\lambda$ is the wavenumber of the radiation. For a ^{57}Fe atom, $Z = 26$ and $\lambda = 0.86$ Å for the 14.413 keV transition. This yields the following values:

$$\sigma_{\text{Thomson}} = 1.73 \times 10^{-23} \text{ cm}^2/\text{atom}$$

$$\sigma_{\text{nuclear}} = 2.56 \times 10^{-18} \text{ cm}^2/\text{resonant nucleus}$$

When the concentration of resonant nuclei is low, the Thomson scattering will be relatively important compared to nuclear resonant scattering and both processes should be taken into account. However, if enriched samples are used, the contribution of Thomson scattering to the holographic intensity pattern will be negligible as compared to the nuclear scattering because of the large difference in scattering cross-section.

Chapter 11

Nuclear Emission Holography

In this chapter, a possible experiment for nuclear emission holography is considered. The most crucial part is the sample preparation. One needs a good crystalline sample that is highly enriched in a Mössbauer isotope and in which the radioactive source nuclei can be introduced. In practice, there will be many source nuclei in the sample. In order to obtain a single hologram the following conditions have to be satisfied:

1. the environment of every source nucleus has to be the same, and oriented in the same way
2. the size of the sample has to be much smaller than the sample-detector distance
3. radiation emitted by different source nuclei has to be incoherent

Under these conditions, separate but identical holograms are simply added. If condition (1) is not satisfied, both the hologram and its subsequent reconstruction represent averages over all source nuclei and their near neighbors. In the case of internal γ-ray emitters, the third requirement is always fulfilled. The deexcitation of a source nucleus is a stochastical process which is uncorrelated with a similar event at another source nucleus. As a result, the radiation emitted by different sources is incoherent and cannot interfere.

The most appropriate Mössbauer isotope for nuclear emission holography (and for nuclear resonant scattering in general) is ^{57}Fe. The 14.413 keV transition from the first excited state to the ground state provides radiation with sufficiently short wavelength ($\lambda = 0.86$ Å) to allow holography with atomic resolution. Moreover, highly enriched crystalline samples can be prepared by molecular beam epitaxy. There is also a parent isotope, ^{57}Co, which can be used to generate the source radiation. The ^{57}Co nuclei can be introduced into the sample either during growth by co-deposition, or after growth by thermal diffusion or ion implantation.

The formulae in the previous chapters describing nuclear emission holography have been derived for a single transition energy, which implies no hyperfine splitting of the nuclear levels. This has two important consequences. If the source nucleus is not subjected to hyperfine interactions, the emitted radiation pattern is isotropic. Moreover, no polarization effects should be taken into account, so that the resonance condition between source and scattering nuclei is easily satisfied.
In this chapter, two possible samples for nuclear emission holography are proposed. The first one is a single-line sample containing ^{57}Fe, which would benefit from the two properties mentioned above. The second is a thin layer of α-^{57}Fe, which, although it is hyperfine split, has the advantage that it can easily be made into a γ-ray source for nuclear emission holography.

Assuming the ^{57}Co ions are introduced into the sample by ion-implantation, an estimation for the data collection time is made. It turns out that a nuclear emission hologram can be obtained in a reasonable time.

Finally, in the last section, the reconstruction procedure to obtain a three-dimensional real-space image of the nuclear environment is explained and discussed.

11.1 Sample Preparation

As a possible sample for nuclear emission holography, a metastable monosilicide can be considered. By co-deposition at room temperature a cubic FeSi phase can be grown epitaxially on a Si(1 1 1) substrate. A detailed study [126] has shown that these films exhibit an excellent crystalline quality up to a thickness of 1000 Å. The FeSi has a CsCl structure with a lattice parameter ($a_0 = 2.77$ Å). Due to the cubic symmetry around the ^{57}Fe probe atoms, a single-line spectrum in conversion electron Mössbauer spectroscopy (CEMS) is observed. However, this single-line structure breaks up when the sample is heated above 300°C [126]. As a function of the annealing temperature a gradual transition from the cubic FeSi phase to a polycrystalline ϵ-FeSi phase occurs. This can be deduced from figure 11.1.

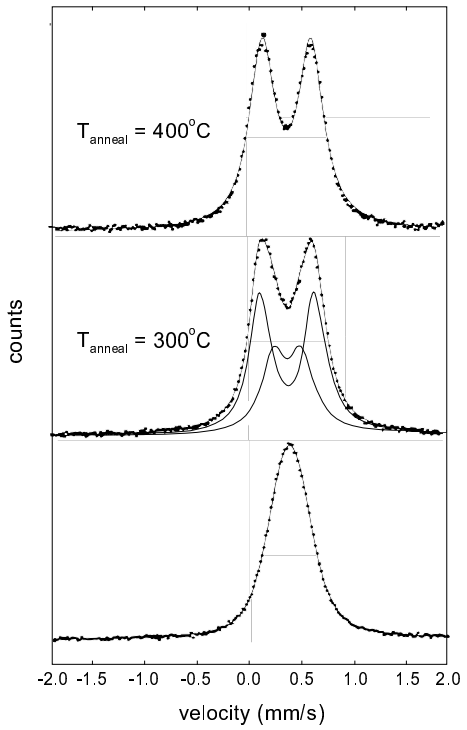

Figure 11.1: In-situ Cems spectra at room temperature of a 650 Å FeSi[CsCl] film on Si(1 1 1) after growth and after annealing at 300°C and at 400°C [126].

The ^{57}Co source nuclei can be introduced into the FeSi film by ion implantation. For nuclear emission holography one needs thin samples in order to minimize the influence of long-range coherence effects. Therefore, low implantation energies are preferred which yield a smaller implantation range. Figure 11.2 displays the implantation profile for ^{57}Co implanted into FeSi at 40 keV, simulated with the TRIM program [127]. The average implantation depth is 205 Å and the average straggling is 92 Å. A 400 Å FeSi[CsCl] layer will stop approximately 97% of all ^{57}Co ions and can be considered as a sample for nuclear emission holography.

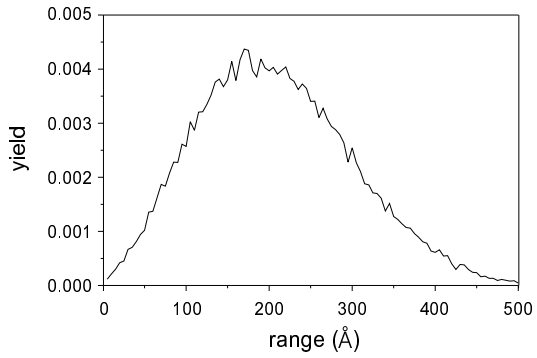

Figure 11.2: TRIM simulation for the implantation profile of ^{57}Co in a FeSi layer at 40 keV.

When the source nuclei are implanted into the sample, care should be taken to minimize damage to the crystalline structure. This is a crucial point for holography experiments. Most damage can be restored by annealing the sample after implantation. However, as mentioned before, annealing above 300°C will cause an irreversible phase transition from the cubic FeSi[CsCl] to ϵ-FeSi which is polycrystalline. As a consequence, annealing of the sample is limited to 300°C.
On the other hand, implantation may cause a local heating of the crystal near the end position of the ^{57}Co ions. This might also induce the phase transition. Too little is known about Co implantation into FeSi[CsCl] to predict the result. A more profound study needs to be done on this topic.

Another candidate sample for nuclear emission holography is a thin epitaxial ^{57}Fe layer which can be annealed after ^{57}Co implantation. Such a layer has a bcc structure and the implanted Co ions will preferentially occupy substitutional lattice positions. The maximum allowed implantation dose in order not to damage the crystalline structure of the target is approximately 5×10^{13} ions/cm^2. Due to contamination of the mass M = 57 by Fe, only a fraction ($\approx$ 25%) of this number will be ^{57}Co ions.

(For a 1 cm^2 sample this dose corresponds to a 10 μCi source.) A small drawback is the hyperfine splitting in α-Fe. This will cause the emitted radiation pattern to be anisotropic and, more relevant for the application in nuclear holography, the holographic effect will be a factor of two smaller. This can be understood as follows. The ground state of ^{57}Fe is split into two sublevels. Initially, the source nucleus is in an excited state and will deexcite by a magnetic dipole transition to one of the two ground states. See figure 11.3. The emitted radiation can be resonantly absorbed and reemitted only by ^{57}Fe nuclei that are in the same ground state. ^{57}Fe nuclei that are in the other ground state do not fulfill the resonance condition and cannot resonantly scatter the photon produced by the source. Since at room temperature equal population of both ground states can be assumed, the effective number of resonant nuclei is 50% of the total number of ^{57}Fe nuclei. The effect scales with the number of resonant nuclei and thus will also be reduced by $\approx 50\%$.

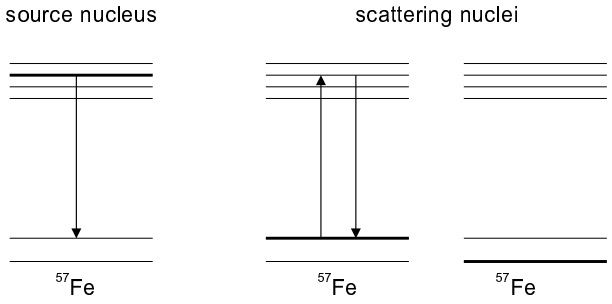

Figure 11.3: Scheme for resonant scattering of radiation produced by a source nucleus, in the presence of hyperfine interactions.

11.2 Recording of Hologram

The radioactive ^{57}Co ions implanted into the sample will decay via electron capture to ^{57}Fe. The subsequent decay scheme is shown in figure 11.4. 89.3% of all ^{57}Co decays will go via the 14.413 keV level of ^{57}Fe. However, due to the high internal conversion coefficient ($\alpha = 8.19$) only 10.9% of this fraction will emit a γ-quantum. The emitted electrons can be absorbed by a thin Al foil in front of the detector. In the radiative decay of the excited ^{57}Fe nucleus, not only 14.413 keV quanta are created, but also 136.475 keV and 122.062 keV gamma-rays. These do not participate in the resonant scattering process and will not contribute to the holographic signal. However, one should avoid their detection, because they will increase the background in the hologram.
The best way to record the hologram would be to use a position sensitive and energy selective detector. An alternative could be an energy selective detector which is placed sequentially at different positions on the hemisphere, but this solution requires very long data collection times. Another alternative is a position sensitive detector with low efficiency at high energies.

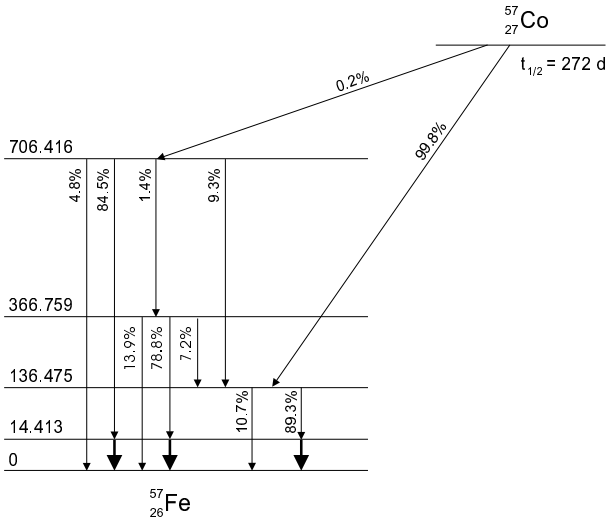

Figure 11.4: Decay scheme of ^{57}Co. The numbers at the left indicate the energies in keV of the ^{57}Fe nuclear levels relative to the ground state. The other numbers refer to the branching ratios for the different decay processes. Data are taken from [128].

11.2.1 Data Acquisition Time

For a specific ^{57}Co implantation dose D, the number of 14.413 keV quanta emitted after time t into the opening angle $\Delta\theta \times \Delta\theta/\sin\theta$ is given by

$$N(t) = b\,\frac{\gamma_R}{\Gamma}\,D\,\left(1 - e^{-t/\tau}\right)\,\frac{(\Delta\theta)^2}{4\pi}$$

where $b = 89.3\%$ is the branching ratio for the 14.413 keV transition, $\gamma_R/\Gamma = 10.9\%$ is the percentage of radiative decay for this transition and $\tau = 384$ days, is the radioactive lifetime of ^{57}Co. To obtain the number of detections in $\Delta\theta \times \Delta\theta/\sin\theta$, one should multiply the above expression by η, the efficiency of the detector at 14.413 keV.

Since the minimum number of counts per pixel scales with the inverse of the effect squared, the minimum data acquisition time is determined by the expression

$$\frac{1}{(\alpha\,\epsilon)^2} \leq \eta\,b\,\frac{\gamma_R}{\Gamma}\,D\,\left(1 - e^{-t/\tau}\right)\,\frac{(\Delta\theta)^2}{4\pi} \tag{11.1}$$

where ϵ is the effect (signal-to-background ratio) one wants to measure within an accuracy of α.

Eq. (11.1) can be refined in the case where some a priori knowledge about the crystalline structure is available. The crystal symmetry will be reflected in the holographic intensity pattern. If an s-fold symmetry is known beforehand, the hologram can be symmetry-averaged so that the minimum counts per pixel will be scaled by s. E.g., in case of a bcc lattice, the holographic image has an 8-fold symmetry. For such cases the minimum data acquisition time is given by the equation

$$\frac{1}{s}\,\frac{1}{(\alpha\,\epsilon)^2} = \eta\,b\,\frac{\gamma_R}{\Gamma}\,D\,\left(1 - e^{-t_{\min}/\tau}\right)\,\frac{(\Delta\theta)^2}{4\pi} \tag{11.2}$$

Or, solving Eq. (11.2) for $t_{\min}$:

$$t_{\min} = -\tau\,\ln\left[1 - \left(s\,(\alpha\,\epsilon)^2\,\eta\,b\,\frac{\gamma_R}{\Gamma}\,D\,\frac{(\Delta\theta)^2}{4\pi}\right)^{-1}\right] \tag{11.3}$$

In expression (11.3), an energy selective detector has been assumed so that the contribution to the detected signal of gamma quanta with an energy different from 14.413 keV is zero.

From the simulations in chapter 10 for a bcc lattice of ^{57}Fe it follows that the holographic effect is $\epsilon \approx 6\%$ and the required resolution in the order of $\Delta\theta \approx 1°$.

Consider now the case of a bcc ^{57}Fe sample in which 5×10^{12} ^{57}Co ions are implanted. Without any a-priori knowledge about the crystalline symmetry after implantation, the minimum data acquisition time for nuclear emission holography can be estimated. For a position sensitive, energy selective detector which only registers 14.413 keV quanta, the required data acquisition time will be relatively short. E.g., with a detector efficiency at 14.413 keV of 15%, a nuclear emission hologram with an accuracy of 10% is obtained after six days.

However, if the detector also registers higher energies, then Eq. (11.3) should be replaced by

$$t_{min} = -\tau \ln \left[1 - \left(s \, \alpha \, \epsilon'^2 \sum_i \eta_i \, b_i \left(\frac{\gamma_R}{\Gamma} \right)_i D \, \frac{(\Delta\theta)^2}{4\pi} \right)^{-1} \right]$$

The summation runs over all detected energies. The detector efficiency for each energy is given by η_i. b_i and $(\gamma_R/\Gamma)_i$ are the branching ratio and the probability for radiative decay of the corresponding nuclear transition. The signal-to-background ratio ϵ' will be decreased due to the detection of higher energies. An explicit expression for ϵ' is given by

$$\epsilon' = \epsilon \, \frac{\eta \, b \, \gamma_R/\Gamma}{\sum_i \eta_i \, b_i \, (\gamma_R/\Gamma)_i}$$

For the samples under consideration, the contribution of higher energies to the detected signal will mainly be due to the 122.062 keV transition in ^{57}Fe. The minimum data acquisition time increases rapidly when the detector efficiency at this energy increases.

11.3 Reconstruction

The next step after having recorded the nuclear emission hologram, is to reconstruct the three-dimensional real-space image of the nuclear environment of the source. Therefore, one should illuminate the normalized hologram $F(\hat{k})$ with the conjugate of the reference wave, which is a converging spherical wave. Such a process may not be practical, but one can compute the image intensity numerically following the procedure explained in Refs. [100, 101]. In a region within a few interatomic spacings of the origin, the image wave field may be determined from the integral:

$$U(\vec{r}) = \int\int_S d\sigma_{\hat{k}_0}\; F(\hat{k})\, e^{-i\vec{k}_0\cdot\vec{r}} \tag{11.4}$$

with $\vec{k}_0 = \hat{k}\,\omega_0/c$. The surface integral runs over the available angular range of the hologram. It yields the image amplitude at the position $\vec{r}(x,y,z)$. The image intensity is then given by $|U(\vec{r})|^2$.

Inserting Eq. (10.2) for $F(\hat{k})$ into Eq. (11.4) and expanding the sine as exponentials yields:

$$\begin{aligned} U(\vec{r}) \;=\; -\frac{\gamma_R}{\Gamma}\,\frac{1}{2i}\sum_m \Bigg\{ & \frac{e^{i\,\omega_0\, r_m/c}}{\omega_0\, r_m/c}\int\int_S d\sigma_{\hat{k}_0}\; e^{-i\vec{k}_0\cdot(\vec{r}_m+\vec{r})} \\ & -\frac{e^{-i\,\omega_0\, r_m/c}}{\omega_0\, r_m/c}\int\int_S d\sigma_{\hat{k}_0}\; e^{-i\vec{k}_0\cdot(-\vec{r}_m+\vec{r})}\Bigg\} \end{aligned}$$

The exponential factors $e^{-i\vec{k}_0\cdot(\pm\vec{r}_m+\vec{r})}$ will oscillate as $\hat{k}$ explores the hologram and for most values of $\vec{r}$ the integral will give a very small image amplitude. But, when $\vec{r} \approx \pm\vec{r}_m$ the exponents are near one and a large contribution to the image is obtained. Since $\vec{r}_m$ corresponds to the position of a resonant nucleus, the reconstructed image will show high intensity spots near nuclear positions. Apart from the real image one will also get twin images, well known in holography [91]: for every $\vec{r}_m$ the reconstructed image will show a twin nucleus at $-\vec{r}_m$.

The appearance of the twin images can be very troublesome in γ-ray holography. It will not only yield a reconstructed image intensity at positions $-\vec{r}_m$ which do not necessarily correspond to positions of scattering nuclei, the overlap of real and twin images can also cause the reconstructed image

intensity to be enhanced or suppressed. For certain combinations of kr_m the image of the scattering nuclei may even vanish completely, so that certain scattering nuclei cannot be viewed at all [109].

Several techniques have been proposed to remove the twin images. In Ref. [114] a solution is provided by recording several holograms at different energies. By properly combining the complex wave fields reconstructed from the holograms at several wave numbers, the contribution from twin images can be greatly reduced and the image resolution can be substantially improved [103]. However, this multiple-energy reconstruction algorithm cannot be applied to nuclear holography because here the energy of the γ-ray is determined by the nuclear transition and cannot be varied over a wide range.
An alternative approach for nuclear absorption holography with γ-radiation is described in Ref. [125]. It exploits the fact that the nuclear scattering phase depends strongly on the energy deviation from exact resonance. By recording holograms at two energies that are symmetrically detuned from resonance and by performing a properly phased summation of the reconstructed images, cancellation of real and twin images can be avoided. Again, this solution is not applicable to nuclear emission holography because the energy of the emitted radiation cannot be (de)tuned.
Other reconstruction techniques, involving scattering amplitude and phase-compensation schemes, have also shown to improve the image quality [129, 130], but require knowledge of the scattering amplitude.

Returning now to Eq. (11.4), it can be written in terms of k_x and k_y, the coordinates determining the unit vector $\hat{k}$:

$$U(x,y,z) = \int_{-1}^{1} dk_x \int_{-\sqrt{1-k_x^2}}^{\sqrt{1-k_x^2}} dk_y \; F(\hat{k}) \; e^{-i\,z\sqrt{1-k_x^2-k_y^2}\,\omega_0/c}$$

$$\times\, e^{-i\,x\,k_x\,\omega_0/c} \; e^{-i\,y\,k_y\,\omega_0/c} \qquad (11.5)$$

This formula looks very much like a Fourier integral. However, there is a subtle difference because a two-dimensional hologram is transformed into a three-dimensional space image. The third dimension is obtained by multiplying the normalized holographic image with an appropriate phase factor before performing the two-dimensional Fourier transform.

In this reconstruction procedure, the two-dimensional phased Fourier transform is applied to the normalized holographic intensity $F(\hat{k})$. This function is calculated from the nuclear emission hologram by subtracting the intensity of the reference wave $I^{00}(\hat{k})$ and normalizing to it. The reference wave

intensity can be derived from the experimental data using the appropriate criteria. For example, in the case of nuclear emission holography on a single-line sample, the reference wave emitted by the source nucleus is isotropic and, hence, $I^{00}(\hat{k})$ will be constant. This constant can be approximated by the mean holographic intensity. If the reference wave is not emitted isotropically, $I^{00}(\hat{k})$ should be determined in a different way. See, e.g., Refs. [106, 125]. If, on the other hand, $I^{00}(\hat{k})$ cannot be determined experimentally, one can transform the total measured intensity $I(\hat{k})$. Including the reference wave only gives an additional intensity contribution near the origin of the reconstruction [99].

Chapter 12

Conclusions

The concept of nuclear emission holography has been explored. In this method, radioactive nuclei are located inside the lattice. By recording the emitted radiation as a function of the direction, three-dimensional information on the local environment of these nuclei can be obtained. The minimal resolution in the reconstructed image is determined by the wavelength of the γ-rays, but also by the source size and the detector resolution.

In this work, a quantum mechanical theory to describe nuclear emission holography has been derived in the single-scattering approximation. The result is a very transparent formula for the contrast function. By means of simulations for a bcc lattice of ^{57}Fe, the feasibility of nuclear emission holography has been shown. A holographic effect in the order of a few percent is expected, which would correspond to a data collection time of a few days if a position sensitive and energy selective detector is used. The aim is to obtain three-dimensional information on the local environment of the source nuclei. However, as has been shown, all resonant nuclei in the sample will contribute to the signal. By applying an appropriate low-pass filter on the measured holographic intensity pattern, a limited volume around the source nucleus can be chosen.

In a nuclear emission holography experiment, the most crucial step will be the sample preparation. First of all, one needs an enriched crystalline sample. Secondly, the radioactive source nuclei should be introduced into the sample in sufficient amount and without damaging the crystalline structure. Moreover, in order to obtain a nice hologram, the source nuclei should occupy well-defined positions with only a small number of inequivalent sites. Otherwise, the structure in the hologram will disappear because of the superposition of many different intensity patterns.

Nuclear holography, both in the direct and in the reversed version, is only sensitive to the positions of the resonant nuclei. It has the possibility to separate the Mössbauer nuclei in the three-dimensional reconstructed image. This can be a real advantage over other structural characterization techniques when one is only interested in this subset of nuclei.

The main advantage of nuclear emission holography compared to X-ray scattering techniques is that smaller structures can be studied. This is a consequence of the fact that the cross-section for nuclear resonant scattering is many orders of magnitude larger than the cross-section for X-ray diffraction or X-ray scattering on electrons. Similarly, nuclear emission holography has the same advantage over nuclear absorption holography (the reversed version of nuclear holography with internal sources) because the latter technique requires not only nuclear resonant scattering, but also absorption of the γ-ray. Again, thicker samples are required in order to get enough absorption. On the other hand, nuclear absorption holography has the advantage over nuclear emission holography that it can be tuned to a particular Mössbauer transition because the γ-ray source is located outside the sample and can be Doppler modulated. As a result, it is possible to select a defined set of hyperfine interaction parameters and to visualize not only the crystallographic structure of the resonant nuclei, but also the magnetic structure.

Typical examples of nuclear emission holography can be the study of low-dimensional structures, such as small clusters, very thin epitaxial layers or nuclei at an interface, where the interest goes primarily to the positions of the resonant nuclei.